Proceedings of the Combustion Institute 42 (2026) 106224

Contents lists available at ScienceDirect

Proceedings of the Combustion Institute

journal homepage: www.elsevier.com/locate/proci

On the role of oxide layer thickness in iron particle cloud ignition: A carrier-phase DNS study

Parsa Ghofrani [a,*], Sheu Her Tey [a], Luis Felipe Rico Cortes [a], Xiaocheng Mi [b], Oliver Thomas Stein [c], Andreas Kempf [a]

[a] Chair of Fluid Dynamics, Institute for Energy and Materials Processes, University of Duisburg–Essen, Germany
[b] Department of Mechanical Engineering, Eindhoven University of Technology, The Netherlands
[c] Engler-Bunte-Institut, Simulation of Reacting Thermo-Fluid Systems, Karlsruhe Institute of Technology, Germany

ARTICLE INFO

Keywords:
Iron combustion
Ignition
Carrier-phase direct numerical simulation
Solid fuel combustion

ABSTRACT

Carrier-phase direct numerical simulations (CP-DNS) of a three-dimensional turbulent mixing layer are performed to investigate how the ignition characteristics of iron particles affect the overall combustion. The particle heat-up rate and the oxide layer thickness are shown to be key factors controlling ignition success, highlighting the importance of thermal coupling between particles and the surrounding hot gases. Slow particle heat-up does not initiate ignition immediately, but causes a build-up of oxide layer thickness, increasing the temperature required for ignition and leading to particle ignition failure. Thereby, the ignition temperature of particles was found to increase from nearly 1200 K to just above 1600 K, far above the temperature of the hot gas. This increase in ignition temperature to values higher than the hot gas temperature hinders the further ignition of particles and the formation of iron flames. A particle-driven gas-phase flame is observed only under preheated condition that promotes particle ignition and the formation of a diffusion-like flame front. These findings provide new insights into the processes that determine flame stabilization in iron particle combustion and provide a reference for the further development of iron combustion modeling.

Novelty and significance statement: The formation of a self-sustained iron flame fundamentally relies on the successful ignition of individual particles. The ignition behavior of iron particles is governed by solid-state oxidation kinetics and can be influenced by the oxide layer thickness (Mi et al., 2022). Although significant progress has been made in studying single-particle ignition, limited data exist on how the ignition dynamics are affected in a turbulent flow. We present a comprehensive study on iron particle ignition dynamics in turbulent flows affected by oxide layer thickness by means of three-dimensional direct numerical simulations of a turbulent mixing layer. Additionally, the high-fidelity DNS datasets generated here provide valuable reference data for future model development.

1. Introduction

Iron oxide reduction and subsequent combustion present a promising pathway for energy storage and retrieval. Iron powder can be oxidized to release energy and later regenerated using renewable hydrogen, enabling a sustainable cycle without any toxic or hard to handle fuels, oxidizers or intermediates. Its solid-state nature simplifies storage and transportation, making it an interesting alternative for industrial applications requiring high-temperature [1].

A detailed analysis of the combustion processes is crucial to design a real-world combustor. In particular, ignition dynamics of iron particles are one of the key factors controlling combustion and flame stabilization. At the current time, some valuable research has been conducted on single particle combustion, but there are few data showing if and how this single particle ignition affects the overall flame stabilization. We aim to take a step forward to address this issue with the present paper. The ignition temperature of micron-sized iron particles has been measured experimentally in recent studies [2–5]. Ning et al. [2] investigated single particle ignition in a flame generated hot coflow setup. Ignition temperatures between 1030 K and 1130 K, independent of particle size and oxygen concentration were observed. Cen et al. [3]

* Corresponding author.
E-mail address: parsa.ghofrani@uni-due.de (P. Ghofrani).

https://doi.org/10.1016/j.proci.2026.106224
Received 15 March 2026; Accepted 7 June 2026
Available online 7 July 2026

observed similar ignition temperatures in a comparable setup. The ignition temperatures were also measured in an electrically heated drop-tube by Chang et al. [4], showing consistent findings.

These single-particle measurements help to understand the particle-scale physical processes and combustion model development. Hazenberg et al. [6] introduced a first-order kinetic model that captured key features of iron dust flames. This model was later improved by Thijs et al. [7] and Mich et al. [8] by improving heat and mass transfer treatments. In parallel, Mi et al. [9] developed a solid-phase oxidation model for iron particles using a parabolic rate law, consistent with diffusion-controlled solid-state oxidation. Because ignition is governed by this mechanism, their model accurately predicted experimentally reported ignition temperatures. They further demonstrated that ignition temperature and ignition delay time are strongly influenced by the oxide layer thickness. Cen et al. [3] later used Mi's [9] model in their numerical study, and found it to be highly consistent with their experimental measurement as well.

However, detailed measurements of turbulent iron particle combustion remain challenging, making numerical simulations essential. Since LES and RANS still lack validation data, DNS remains essential. However, fully-resolved DNS is computationally expensive and limited to single or a few particles [7,10,11]. An alternative is carrier-phase DNS (CP-DNS) in which a point-particle assumption is used.

CP-DNS has been applied to volatile-containing solid fuels, including coal and biomass [12,13]. More recently, Luu et al. [14,15] carried out CP-DNS of monodisperse and polydisperse iron particle clouds in a turbulent mixing layer and demonstrated that local oxygen depletion strongly limits the overall conversion process. Hemamalini et al. [16] investigated the effects of preferential concentration using CP-DNS. The particle size was found to affect preferential concentration strongly, with small iron particles burning in a laminar-like regime while larger particles induce turbulence. However, in these studies, the oxide-layer thickness was not considered or temperatures were high enough that oxide-layer effects were negligible. Consequently, the influence of oxide-layer–controlled ignition on flame stabilization remains insufficiently explored, neglecting the important flame stabilization that is often hard to achieve in solid-fuel systems.

In this study, we aim to investigate the ignition dynamics of an iron particle cloud in a turbulent mixing layer by means of CP-DNS. Particularly, we incorporated Mi's [9] parabolic oxidation rate law in the particle sub-model and investigated ignition and the role of oxide layer thickness on it. This work seeks to elucidate the mechanisms responsible for ignition and flame stabilization in turbulent flows and to provide reference for the further progress in iron combustion modeling.

2. Particle phase modeling

2.1. Oxidation models

The heterogeneous oxidation of iron is represented through the reaction:

$$Fe_{(c)} + 0.5O_{2\,(g)} \rightarrow FeO_{(c)}$$

This process is described by either Mi's solid–oxide layer diffusion (SOLD) [9] model, in which oxidation is controlled by ionic diffusion through the oxide layer, or the first–order surface kinetics model (FOSK).

2.1.1. First-order kinetics (FOSK)

The model assumes a first-order surface reaction in quasi-equilibrium with diffusion, and is implemented following Mich et al. [8]. The balance between diffusion and reaction is quantified using normalized Damköhler number $\mathrm{Da}^* = (1 + A_p k_d / A_r k_r)^{-1}$. The reaction rate is calculated as $k_r^{\mathrm{FOSK}} = k_0 \exp(-T_a/T_p)$ from particle temperature T_p. Reactive area is defined $A_r = A_p Y_{\mathrm{FeO}}$ using iron oxide mass fraction Y_{FeO} and particle area A_p. The rate constant k_0 and activation temperature T_a are tabulated in Table 1. The mass transfer coefficient k_d is obtained from Sherwood number described in later section. Thereby, the rate of oxidation $\dot{m}_p^{\mathrm{FOSK}}$ is calculated using the external rate of oxygen diffusion $\dot{m}_{\mathrm{O_2,diff}}$ and oxygen density $\rho_{\mathrm{O_2}}$ as follows:

$$\dot{m}_p^{\mathrm{FOSK}} = \dot{m}_{\mathrm{O_2,diff}}\,\mathrm{Da}^* = A_d\, k_d\, \rho_{\mathrm{O_2}}\,\mathrm{Da}^* \tag{1}$$

The FOSK model under-predicted ignition temperature; hence, the Arrhenius constants were recalibrated using ignition temperature measurements [17]. This version is referred to as FOSK-RC.

Table 1
Arrhenius rate constants of each oxidation model.

Model	k_0	T_a (K)
SOLD	2.67×10^{-4} (m^2/s)	20.319×10^3
FOSK	75×10^5 (m/s)	14.4×10^3
FOSK-RC	2.0×10^{10} (m/s)	31×10^3

2.1.2. Solid oxide layer diffusion (SOLD)

The model defines an oxidation rate that is inversely proportional to the oxide layer thickness X_{FeO}. Assuming a thin oxide layer thickness X_{FeO}, the oxidation rate reads:

$$\dot{m}_{\mathrm{p}}^{\mathrm{SOLD}} = \frac{M_{\mathrm{O_2}}}{2M_{\mathrm{FeO}}} \frac{\rho_{\mathrm{FeO}}}{X_{\mathrm{FeO}}} A_p\, k_r^{\mathrm{SOLD}} \tag{2}$$

M_{FeO}, $M_{\mathrm{O_2}}$, ρ_{FeO}, T_p denote molecular weights of iron oxide and oxygen, iron oxide density, and particle temperature, respectively. k_r^{SOLD} is calculated using the constants defined in Table 1. External oxygen diffusion to the particle surface sets the upper bound for the oxidation rate. The SOLD model describes the solid-state oxidation and predicts an infinite rate at the onset of ignition. Therefore, after ignition or melting, the model switches to diffusion-limited mode: $\dot{m}_{\mathrm{p}}^{\mathrm{SOLD}} = \dot{m}_{\mathrm{O_2,diff}}$. For a detailed formulation, see Mi et al. [9]. The normalized Damköhler number, can be therefore obtained as:

$$Da^* = \frac{\dot{m}_p}{\dot{m}_{O_2,\mathrm{diff}}} \tag{3}$$

2.2. Conservation equations

The dispersed iron particles are modeled in a Lagrangian framework under the point-particle assumption. Each particle is assumed to be spherical, subject only to drag force, and is thermally uniform. Gravity has been neglected to keep the results general and transferable, as in a real flame, the effect of gravity would depend on burner direction and the location in the flame. Using interpolated gas-phase quantities u_g and T_g, the governing equations for particle velocity u_p and temperature T_p are:

$$\frac{du_p}{dt} = \frac{u_g - u_p}{\tau_p};\quad \tau_p = \frac{\rho_p\, d_p^2}{18\mu_f} \frac{1}{(1 + 0.15\mathrm{Re}_p^{2/3})} \tag{4}$$

$$m_p c_p \frac{dT_p}{dt} = \underbrace{h_{\mathrm{conv}} A_p (T_g - T_p)}_{\text{convection}} + \underbrace{\dot{Q}_c}_{\text{combustion}} + \underbrace{\frac{dm_p}{dt} h_{s,\mathrm{O_2}}}_{\mathrm{O_2\ formation}} + \underbrace{\epsilon_p \sigma_s A_p (T_{\mathrm{rad}}^4 - T_p^4)}_{\text{radiation}} \tag{5}$$

The momentum relaxation time τ_p is calculated using particle Reynolds number Re_p, particle density ρ_p, and viscosity μ_f. In the energy balance equation, A_p denotes particle surface area, ϵ_p the particle's emissivity and σ_s is the Stefan–Boltzmann constant. A constant radiative background temperature of $T_{\mathrm{rad}} = 300\,\mathrm{K}$ is considered.

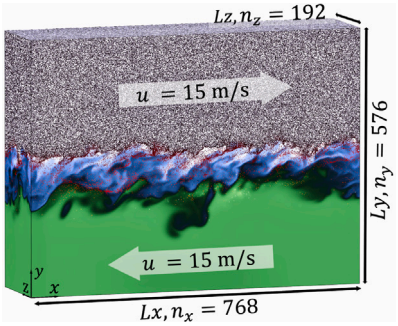

Fig. 1. CP-DNS setup: Snapshot of the gas temperature field with iron particles.

The convective heat transfer coefficient h_{conv} and the mass diffusion coefficient k_d are evaluated from the Nusselt and Sherwood numbers [18] using the thermal conductivity λ_f and the oxygen diffusivity $D_{\text{O}_2,f}$ as follows:

$$\text{Nu} = \frac{h_{\text{conv}}\, d_p}{\lambda_f} = 2 + 0.552\, \text{Re}_p^{1/2}\, \text{Pr}^{1/3} \tag{6}$$

$$\text{Sh} = \frac{k_d\, d_p}{D_{\text{O}_2,f}} = 2 + 0.552\, \text{Re}_p^{1/2}\, \text{Sc}^{1/3} \tag{7}$$

3. Gas-phase modeling

The Eulerian gas phase is described following Luu et al. [14,15] using the conservation of mass, momentum, enthalpy and species mass fractions with the inclusion of particles' inter-phase source terms. Following standard nomenclature, the source terms for mass and species, momentum, and enthalpy conservations are calculated as follows:

$$\dot{S}_{\rho,p} = \dot{S}_{\text{O}_2,p} = -\frac{1}{\Delta^3} \sum_i^{N_p} \frac{dm_p}{dt} \tag{8}$$

$$\dot{S}_{u,p} = -\frac{1}{\Delta^3} \sum_i^{N_p} \frac{d(m_p u_p)}{dt} \tag{9}$$

$$\dot{S}_{h,p} = -\frac{1}{\Delta^3} \sum_i^{N_p} \left(\dot{Q}_{\text{conv},p} + \dot{Q}_{\text{O}_2,p} \right) \tag{10}$$

3.1. Computational setup

The turbulent reacting mixing layer setup [14] shown in Fig. 1 consists of an upper stream (us) of cold air at T_{us} that carries iron particles, and a lower stream (ls) of hot air at T_{ls}. The parallel streams have a velocity difference of $\Delta u_x = 30$ m/s and are initialized with an initial momentum thickness $\delta_{\theta,0}$ corresponding to $Re_{\delta_{\theta,0}} = 44.018$ [19].

The domain, $(L_x, L_y, L_z) = (320, 240, 80) \cdot \delta_{\theta,0}$, is discretized with approximately 85 M cubic cells at a resolution of $\Delta = 0.1$ mm. A total of $N_p \approx 10$ M spherical particles, with an initial diameter of 10 µm and oxide layer thickness $X_{\text{FeO}}^{\text{ini}}$ are randomly positioned in the upper stream to obtain an equivalence ratio of $\phi_{\text{us}} = 1$. Isotropic velocity perturbations [20,21] are added to accelerate mixing layer growth. Seven cases are simulated for 10 ms with varying T_{ls} and $X_{\text{FeO}}^{\text{ini}}$ as summarized in Table 2.

To enable longer simulation times without letting the mixing layer interact with the top and bottom boundaries, a domain with double the height is used for two additional cases. The number of particles is also doubled to $N_p \approx 20$M to maintain the particle number density. Initial oxide layer thickness of the particles is $X_{\text{FeO}}^{\text{ini}} = 1$ nm for both cases. The cases differ in their of stream temperatures as described in Table 3. These two cases are simulated for more than 30 ms.

These cases were simulated with our in-house code *PsiPhi* [12,22] using 6334 cores on SuperMUC-NG.

Table 2
The simulated cases.

Model	T_{ls} (K)	T_{us} (K)	X_{FeO} (nm)
FOSK	1300	300	–
FOSK-RC	1300	300	–
SOLD	1300	300	**1**
SOLD	1300	300	**10**
SOLD	1300	300	**100**
SOLD	**1500**	300	10
SOLD	**1700**	300	10

Table 3
Cases simulated on the enlarged domain.

Name	T_{ls} (K)	T_{us} (K)
Non-Preheat (NP)	1700	300
Preheat (P)	1650	550

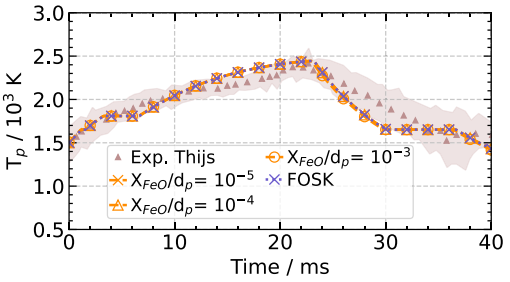

Fig. 2. Temperature evolution for a laser ignited iron particle of diameter $d_p = 54$ µm in 300 K air, comparing the present implementations of SOLD with different oxide layer thicknesses X_{FeO} and FOSK to Thijs's [23] experiment.

4. Validation

4.1. Single particle validation

The iron particle oxidation models are validated by comparing single particle predictions of temperature evolution, burn time and ignition temperature to different experimental measurements.

Fig. 2 illustrates the time evolution of particle temperature for a single laser-ignited iron particle of diameter $d_p = 54$ µm in air at $T_{\text{air}} = 300$ K. Here, simulations using the two oxidation models are compared against Thijs's experimental data [23]. As shown, particle temperature rises from 1500 K and then plateaus at 1810 K due to Fe melting; it subsequently peaks near 2500 K before decreasing and exhibiting another plateau at 1650 K corresponding to FeO solidification. Both oxidation models show identical temperature trajectory. The figure demonstrates good agreement between the current particle oxidation sub-models and experimental results.

Fig. 3 illustrates burn time t_{burn} of a laser-ignited particle under different oxygen concentrations at 300 K. Burn time against particle diameter with different oxide layer thicknesses are shown in each sub-figure, comparing SOLD and FOSK implementations to the experimental measurements of Ning [24]. The predictions of both models agree well with the experimental measurements under all conditions.

Fig. 4 illustrates the critical gas temperature that triggers particle ignition T_g^{ign} for different particle sizes in air (left). Ignition is indicated by thermal runaway as a result of increasing gas temperature as shown in Fig. 4 (right). To account for experimental and numerical uncertainties, the input parameters of the model such as gas temperature, particle diameter, slip velocity and initial oxide layer thickness are sampled randomly to better mimic the experimental conditions. The ignition predictions of FOSK and SOLD along with experimental results [3–5] are shown in Fig. 4 (left). As seen, SOLD prediction of ignition agrees very well at different particle diameters (as also confirmed by the

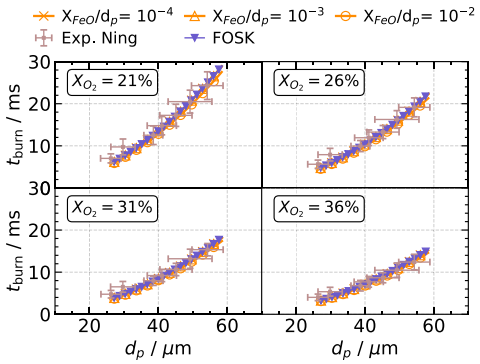

Fig. 3. Burn time t_{burn} of laser-ignited iron particles against diameters d_p for various oxygen concentrations at 300 K, comparing SOLD and FOSK to Ning's [24] experiment.

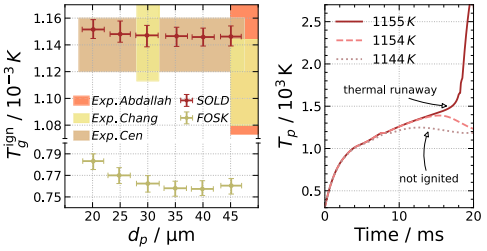

Fig. 4. Left: Ignition temperature depending on particle diameter as predicted by FOSK and SOLD (with oxide layer thickness 70 ± 30 nm) model predictions with experimentally reported ignition temperature ranges. Right: Time evolution of single-particle temperature for a particle burning in air with different temperatures. The ignition predictions of SOLD are compared with different measurements [3–5].

numerical investigation of Cen et al. [3]), whereas FOSK predictions are inconsistent with experiment.

5. Results and discussion

The section is organized as follows: first, the effect of oxide-layer thickness X_{FeO} on single-particle combustion is analyzed; next, particle ignition is examined for the cases in Table 2; finally, gas-phase ignition is studied for the configurations in Table 3.

5.1. Single particle combustion

First, zero-dimensional single-particle combustion is simulated to demonstrate the influence of the reaction models. Ignition is assessed using the particle Damköhler number Da^*, with ignition defined at the particle temperature where $\mathrm{Da}^* = 0.5$. Evolution of particle temperature and reaction progress $C_{\mathrm{ox}} = 1 - m_{\mathrm{Fe}}/m_{\mathrm{Fe}_0}$ are shown for four conditions in Fig. 5. Fig. 5a presents a 10 μm particle ignited at 1600 K in 300 K air, comparing SOLD, and FOSK-(RC). When the particle is ignited, all three models behave similarly. Fig. 5b shows oxidation of a 300 K particle in 1300 K air: all three models predict ignition, but the FOSK(-RC) models predict a significantly shorter (longer) ignition delay. Reducing oxygen to 10% (Fig. 5c) makes FOSK-RC fail to predict the ignition. With the SOLD model, oxidation is independent of oxygen concentration and does not affect ignition success, in line with the experimental observations [2,3]. However, the reaction rate calculated by FOSK depends linearly on the oxygen concentration. The effect of a stepwise increase in gas temperature from 1100 K to 1280 K at 100 ms is illustrated in Fig. 5d: FOSK predicts early ignition, whereas SOLD shows slow oxidation, resulting in an oxide layer thickness growth, while FOSK-RC permits negligible oxidation. After the temperature jump, with SOLD

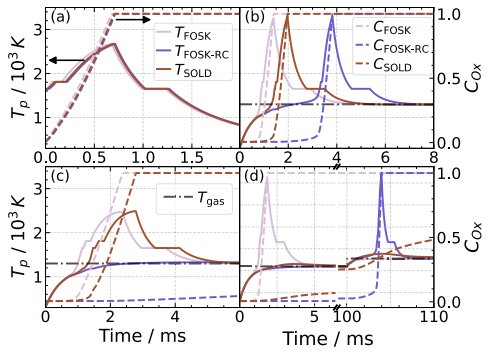

Fig. 5. T and C_{Ox} evolution for 10 μm single particle, for FOSK, SOLD, and FOSK-RC. (a) Ignited particle in 300 K air, (b) 300 K particle in 1300 K air, and (c) in 10% O_2. (d) Air temperature rise from 1100 K to 1280 K at 100 ms.

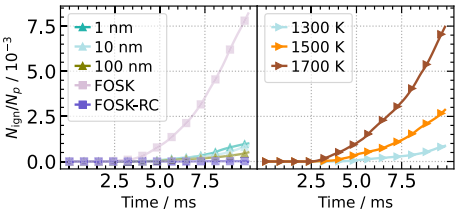

Fig. 6. Evolution of the normalized number of ignited particles for initial oxide layer thicknesses from 1 nm to 100 nm with $T_{\mathrm{ls}} = 1300$ K (left) and lower stream temperatures T_{us} from 1300 K to 1700 K with $X_{\mathrm{FeO}}^{\mathrm{ini}} = 10$ nm (right).

the oxidation accelerates without ignition, while FOSK-RC predicts ignition. Overall, the differences between the FOSK-(RC) models and the oxide-layer-thickness aware SOLD become very apparent. Since the effect of the oxide layer on ignition in SOLD depends on its relative thickness X_{FeO}/d_p as independent parameter [9], similar trends are expected for particle sizes and oxide thicknesses beyond the ranges considered here, provided this ratio remains comparable.

5.2. Particle ignition in turbulent mixing layer

Particle behavior in the three-dimensional simulations of the turbulent mixing layer is considered next. First, Fig. 6 (left) depicts the effect of initial oxide layer thicknesses on the overall ignition of particles. An increase in oxide layer thickness from 1 nm to 10 nm and 100 nm considerably decreases the number of particles ignited. With first-order single-step kinetics (FOSK) the oxide layer thickness would be ignored, leading to too fast (FOSK) or too slow (FOSK-RC) ignition. Fig. 6 (right) shows the effect of lower stream temperature, increasing from 1300 K to 1700 K, resulting in a larger and faster growth in the number of ignited particles.

Fig. 7 (bottom) shows the distribution of ignition temperatures T_{ign} (which is defined as particle temperature T_p where $\mathrm{Da}^* = 0.5$) for initial oxide layers of 1 nm, 10 nm, and 100 nm with $T_{\mathrm{ls}} = 1300$ K. The ignition temperature increases with the initial oxide layer thickness, with T_{ign} from between 1300–1600 K for 1 nm, to between 1500–1600 K for 100 nm. First-order kinetics would predict much lower (or higher) T_{ign}. The inset shows the mean ignition temperature $\overline{T}_{\mathrm{ign}}$ as a function of $X_{\mathrm{FeO}}^{\mathrm{ini}}$. The mean ignition temperature $\overline{T}_{\mathrm{ign}}$ remains at nearly 1450 K when increasing $X_{\mathrm{FeO}}^{\mathrm{ini}}$ from 1 nm to 10 nm, but rises to about 1550 K for 100 nm. The same trend was reported by Mi et al. [9]. Interestingly, the standard deviation of the ignition temperature decreases as $X_{\mathrm{FeO}}^{\mathrm{ini}}$ increases. This is because the thicker oxide layer increases the minimum ignition temperature.

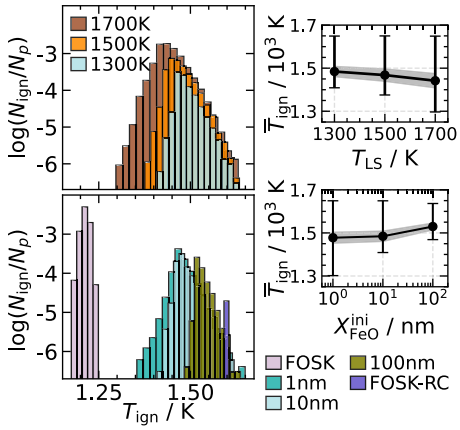

Fig. 7. Distribution of ignition temperature for (bottom) initial oxide layer thickness from 1 nm to 100 nm with T_{ls} = 1300 K, and (top) lower stream temperatures T_{us} from 1300 K to 1700 K with X^{ini}_{FeO} = 10 nm. The insets show mean ignition temperature against the initial oxide layer thickness and the lower stream temperature.

Fig. 7 (top) shows the effect of lower stream temperature on the ignition temperature for an initial oxide layer thickness of 10 nm. As the lower stream temperature increases, the minimum ignition temperature decreases from 1400 K down to 1300 K. The inset shows how with increasing lower stream temperature, the average ignition temperature drops. This results from faster heat-up rates, leaving the oxide layer insufficient time to grow and delay ignition and higher-temperature conditions.

Scatter plots of the ignition temperature T_{ign} versus the change in oxide layer thickness until ignition $X^{ign}_{FeO} - X^{ini}_{FeO}$ are shown in Fig. 8 (left) for different initial oxide layer thicknesses (T_{ls} = 1300 K), and (right) for different lower stream temperatures (X^{ini}_{FeO} = 10 nm). FOSK predictions are also added for reference. Fig. 8 (left) shows that particles with thicker oxide layers tend to ignite at much higher temperatures. Overall, Fig. 8 (right) shows that hotter lower streams, leading to faster heat-up rates, promote ignition at lower temperatures. If such high heating rates cannot be achieved, particles need to have at least a thin oxide layer thickness to ensure ignition. For initial thicknesses of 1 and 10 nm, the increase in T_{ign} with ΔX_{FeO} is similar, but larger than that of 100 nm. Additionally, as oxide-layer growth increases in all cases, the ignition temperatures gradually converge, showing similar values near the upper end of the plot. When the oxide layer becomes very thick, the oxidation rate slows down at a given temperature, causing further oxidation and heat release to stagnate. Consistently, Mi et al. [9] showed that a large ratio of initial oxide thickness to particle radius makes the predicted ignition temperature approach that of a steady-state. Expectedly, the FOSK model prediction of ignition temperature does not scale with oxide-layer thickness and remains around 1200 throughout the simulation.

5.3. Particle driven combustion in turbulent mixing layer

The development of particle-driven combustion in the three-dimensional turbulent mixing layer is investigated in this section. Two cases are considered: non-preheated, with an upper stream temperature of T_{us} = 300 K, and preheated, with T_{us} = 550 K. Fig. 10 illustrates the temporal evolution of the gas temperature and particle oxidation progress C_{Ox} comparing the non-preheated (top row) and preheated (bottom row) cases. As turbulent vortices develop in the mixing layer, particles are driven away from the vortex cores and accumulate outside the vortices, forming streaks of particles. When these particle streaks are entrained into the hot lower stream, the particles heat up, ignite, and release heat, which in turn increases the gas-phase temperature.

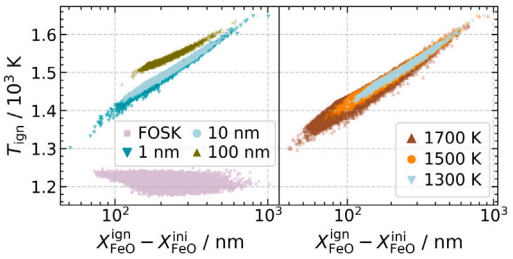

Fig. 8. Scatter plot of ignition temperature T_{ign} versus the change in oxide layer thickness until ignition for (left) initial oxide thicknesses of 1 nm to 100 nm, and (right) lower stream temperatures from 1300 K to 1700 K.

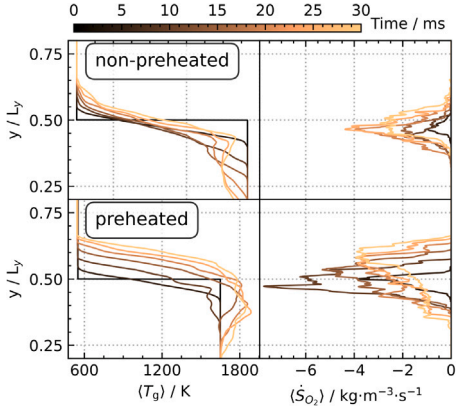

Fig. 9. Spatially-averaged gas temperature $\langle T_g \rangle$ (left) and oxygen consumption rate $\langle \dot{S}_{O_2} \rangle$ (right) for the non-preheated (top) and preheated (bottom) cases at different times.

By 3 ms, the turbulent shear layer starts to develop. In both cases, a number of clockwise-rotating vortices form within the mixing zone, with particles accumulating in clusters away from vortex cores. The vortices in the non-preheated case are slightly smaller in size, which can be attributed to the lower viscosity and higher density of the carrier gas. In the preheated case, at 14 ms, the shear layer is strongly heated, with pockets of hot gas reaching temperatures of nearly 2200 K due to combustion of particle streaks. Elevated temperatures are also observed in the upper stream, where particle clusters accumulate at the interface between the cold and hot streams. In contrast, in the non-preheated case, at the same time, the shear layer does not show an increase in gas temperature but rather a decrease due to mixing; particle clusters remain largely separated from the hot lower stream without noticeable ignition.

By 21 ms, the hot zone in the preheated case has widened and exhibits a more homogeneous temperature distribution. This trend continues at later times: the high temperature zone in the preheated case becomes smoother and extends further into the upper stream. Burning particles (magenta) are observed at the interface between hot and cold gas, resembling a propagating flame front. The non-preheated case, in contrast, does not show any substantial temperature rise in the gas phase and the particle clusters remain spatially separated from the hot gas.

The spatially averaged profiles of gas-phase temperature $\langle T_g \rangle$ and oxygen consumption rate $\langle \dot{S}_{O_2} \rangle$ for the non-preheated (top row) and preheated (bottom row) cases are illustrated in Fig. 9. In both cases, the temperature profiles initially widen, followed by the emergence of a second peak within the mixing layer toward the lower stream, which indicates the onset of group combustion. The oxygen consumption rate profiles support this observation: at early times, they peak near the center of the domain with a narrow spatial spread in both cases,

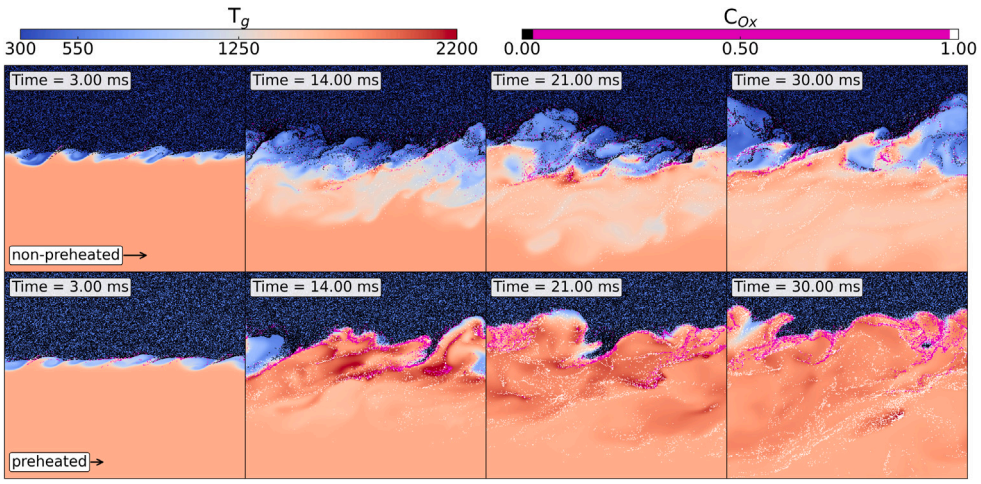

Fig. 10. Snapshots of the gas temperature and particle oxidation in the x-y plane at $z = L_z/2$ for preheated and non-preheated cases. Particles are colored by their oxidation progress.

marking the initial region where oxidation occurs. As the simulation progresses, both the magnitude and width of the oxygen consumption profiles increase, explaining the formation of localized hot temperature pockets due to intensified oxidation. In the preheated case, the second temperature peak appears much earlier, at approximately 7 ms, and reaches significantly higher values of 1850 K. Correspondingly, the oxygen consumption increases before decreasing in peak magnitude while continuing to widen spatially. This behavior is consistent with the smoothing of the temperature fields and the formation of a broader and less intense reaction zone. At the same time, the location of the peak oxygen consumption shifts upward, indicating the upward propagation of the reactive region (flame). This upward spread is also evident in the temperature profiles, with high temperatures extending into the upper stream after approximately 7 ms due to particle combustion at the hot–cold gas interface, resembling a flame-front progression. At later simulation times, the preheated case develops a nearly uniform temperature of approximately 1800 K in the lower stream while continuing to expand upward. To assess whether particle ignition occurs solely due to mixing with the hot lower stream or the combustion of particles triggers ignition of unburnt particles (effectively the existence of a self-sustained, propagating flame), the temperature profiles can be compared with the expected behavior of an inert mixing process in a turbulent shear layer. In such a case, the temperature gradient would gradually smooth out with the lower stream being more affected due to its lower heat capacity in the absence of particles. This smoothing of temperature profiles resembles the behavior observed in the non-preheated case between $y/L_y = 0.5$ and $y/L_y = 0.7$, where almost no oxidation occurs as seen in oxygen consumption figures. However, in the preheated case, the temperature gradient in the upper stream region does not smooth out but instead shifts upward after approximately 14 ms. This behavior cannot be explained by mixing alone and indicates additional heat release from particle combustion, which promotes further ignition of surrounding particles. In contrast, the non-preheated case exhibits a delayed and weaker response. The second temperature peak appears much later, around 20 ms, and remains approximately 25% lower throughout the simulation. The oxygen consumption peak largely stays near the center of the domain, indicating that the reactive region does not propagate upward. Consequently, the temperature increase occurs mainly within the lower stream. By the end of simulation time, non-preheated case maintains a more localized and weaker temperature rise and a decaying oxygen consumption rate with a nearly stationary peak magnitude near the center of the domain.

Fig. 11 illustrates the temporal evolution of the number of ignited particles, normalized by the total number of particles (left axis) and its rate of change (right axis) for the preheated and non-preheated case.

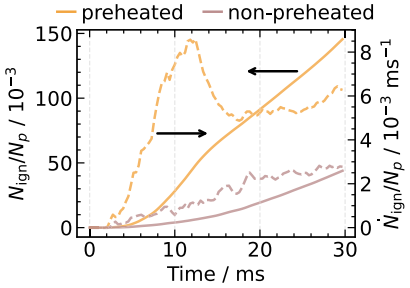

Fig. 11. Temporal evolution of the number of ignited particles, normalized by the total number of particles (left axis), and its rate of change in time (right axis) for preheated and non-preheated case.

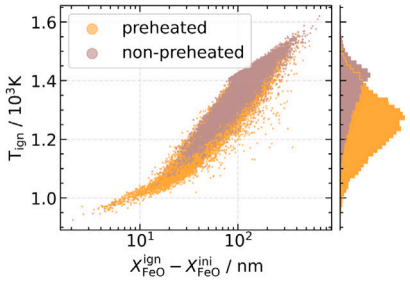

Fig. 12. Marginal plots of ignition temperature T_{ign} versus the change in oxide layer thickness until ignition for preheated and non-preheated cases.

Ignition in the preheated case begins at approximately 6 ms, whereas in the non-preheated case it starts about 2 ms later. The number of ignited particles in the preheated case begins growing at 6 ms with an increasing rate, followed by an approximately linear growth after 12 ms. Subsequently, the ignition rate seems to start increasing again after about 25 ms. In contrast, the non-preheated case shows a delayed and slower growth that begins to stagnate after 20 ms. As a result, by 30 ms, the preheated case contains roughly three times more ignited particles than the non-preheated case.

Marginal plots of ignition temperature T_{ign} against the change in oxide layer thickness until ignition for the preheated and non-preheated cases are shown in Fig. 12. Similar to Fig. 8, the growth of the oxide layer leads to an increase in the ignition temperature. The ignition temperature in the non-preheated case ranges between 1200 K and 1600 K, while the ignition temperature range in the preheated case

is widened to between 1000 K and 1600 K. This is due to the higher gas-phase temperature that promotes faster particle heat-up rates, leaving insufficient time for the oxide layer to grow, consistent with the observation in Fig. 8. Additionally, the higher gas-phase temperature resulting from the iron flame also reduces heat loss from the particles, further promoting ignition. The lower ignition temperatures observed in the preheated case explain its higher propensity for flame formation compared to the non-preheated case.

6. Conclusion

Ignition of iron particle clouds in a turbulent mixing layer and the effect of oxide layer thickness were explored by three-dimensional carrier-phase DNS. The initial zero-dimensional analysis showed that oxide growth strongly governs ignition success and its delay. In the turbulent mixing layer, it is observed that increasing the initial oxide layer thickness from 1 to 100 nm caused substantial changes: ignition was delayed, the number of ignited particles was reduced, and ignition temperatures shifted toward higher values. It was also observed that ignoring the effect of oxide layer thickness in the simpler models can lead to under- or over-prediction of the ignition success and delay. Raising the temperatures limits pre-oxidation and allows lower ignition temperatures. Higher gas temperature also broaden the spread of ignition temperatures, indicating increased coupling between turbulence, particle heating rates, and heterogeneous reactions. The potential formation and stabilization of a particle-driven gas-phase flame is also investigated. Preheating the carrier gas and particles accelerates particle heat-up, promoting ignition and leading to the formation of a diffusion-like flame front that propagates upward. In contrast, the non-preheated case shows no signs of flame formation, as slower particle heating results in higher ignition temperatures that hinder the development of a flame front. Overall, particle heat-up rate and oxide layer thickness are shown to be key factors governing ignition, emphasizing the role of thermal coupling between particles and gas phase. This study also demonstrates that models neglecting oxide-layer kinetics can significantly overestimate ignition propensity.

CRediT authorship contribution statement

Parsa Ghofrani: Original Draft, Methodology, Investigation, Data Curation. **Sheu Her Tey:** Original Draft, Analysis. **Luis Felipe Rico Cortes:** Analysis, Review. **Xiaocheng Mi:** Review. **Oliver Thomas Stein:** Review. **Andreas Kempf:** Review, Supervision, Funding acquisition.

Declaration of competing interest

The authors declare that they have no known competing financial interests or personal relationships that could have appeared to influence the work reported in this paper.

Acknowledgments

We gratefully acknowledge the funding received from International Max Planck Research School for Sustainable Metallurgy (IMPRS SusMet), the Gauss Centre for Supercomputing e.V. for computing time on SuperMUC-NG at LRZ, and support by the Helmholtz Association of German Research Centres (HGF), under Energy, program Materials and Technologies for the Energy Transition (MTET). P.G. is also grateful to T.D. Luu for the countless helpful discussions.

References

[1] J.M. Bergthorson, S. Goroshin, M.J. Soo, P. Julien, J. Palecka, D.L. Frost, D.J. Jarvis, Direct combustion of recyclable metal fuels for zero-carbon heat and power, Appl. Energy 160 (2015) 368–382.
[2] D. Ning, Y. Li, T. Li, B. Böhm, A. Dreizler, Size-resolved ignition temperatures of isolated iron microparticles, Combust. Flame 270 (2024) 113779.
[3] L. Cen, Z. Lyu, Y. Qian, W. Zhong, X. Lu, A detailed experimental and numerical study on the ignition temperature of single micron-sized spherical iron particles, Combust. Flame 272 (2025) 113909.
[4] D. Chang, E.S. Germain, R.M. Erb, X. Mi, J.M. Bergthorson, Y.A. Levendis, An experimental study on the ignition temperature of iron particles in an electrically-heated drop-tube furnace, Fuel 404 (2026) 136199.
[5] M. Abdallah, Y. Shoshin, G. Finotello, L. de Goey, Iron particles ignition in different hot coflow temperatures, Proc. Combust. Inst. 40 (1) (2024) 105261.
[6] T. Hazenberg, J.A.V. Oijen, Structures and burning velocities of flames in iron aerosols, Proc. Combust. Inst. 38 (2021) 4383–4390.
[7] L.C. Thijs, C.E. van Gool, W.J. Ramaekers, J.G. Kuerten, J.A. van Oijen, L.P. de Goey, Improvement of heat- and mass transfer modeling for single iron particles combustion using resolved simulations, Combust. Sci. Technol. (2022).
[8] J. Mich, D. Braig, T. Gustmann, C. Hasse, A. Scholtissek, A comparison of mechanistic models for the combustion of iron microparticles and their application to polydisperse iron-air suspensions, Combust. Flame 256 (2023) 112949.
[9] X.C. Mi, A. Fujinawa, J.M. Bergthorson, A quantitative analysis of the ignition characteristics of fine iron particles, Combust. Flame 240 (2022) 112011.
[10] B.D. Nguyen, A. Scholtissek, T. Li, D. Ning, O.T. Stein, A. Dreizler, C. Hasse, Nanoparticle formation in the boundary layer of burning iron microparticles: Modeling and simulation, Chem. Eng. J. 507 (2025) 160039.
[11] F.H. Vance, A. Scholtissek, H. Nicolai, C. Hasse, Effect of oxidizer composition on flame propagation modes in iron particle clusters, Fuel 381 (2025) 133505.
[12] M. Rieth, A.M. Kempf, A. Kronenburg, O.T. Stein, Carrier-phase DNS of pulverized coal particle ignition and volatile burning in a turbulent mixing layer, Fuel 212 (2018) 364–374.
[13] B. Wang, A. Shamooni, O.T. Stein, A. Kronenburg, A.M. Kempf, P. Debiagi, C. Hasse, Investigation of turbulent pulverized solid fuel combustion with detailed homogeneous and heterogeneous kinetics, Energy Fuels 35 (9) (2021) 7077–7091.
[14] T.D. Luu, A. Shamooni, A. Kronenburg, D. Braig, J. Mich, B.D. Nguyen, A. Scholtissek, C. Hasse, G. Thäter, M. Carbone, B. Frohnapfel, O.T. Stein, Carrier-phase DNS of ignition and combustion of iron particles in a turbulent mixing layer, Flow Turbul. Combust. 112 (2024) 1083–1103.
[15] T.D. Luu, A. Shamooni, A. Kronenburg, D. Braig, J. Mich, B.D. Nguyen, A. Scholtissek, C. Hasse, G. Thäter, M. Carbone, B. Frohnapfel, O.T. Stein, Carrier-phase DNS study of particle size distribution effects on iron particle ignition in a turbulent mixing layer, Proc. Combust. Inst. 40 (2024) 105297.
[16] S. Hemamalini, B. Cuenot, J. van Oijen, X.C. Mi, Numerical study probing the effects of preferential concentration on the combustion of iron particles in a mixing layer, Proc. Combust. Inst. 40 (2024) 105617.
[17] B.-D. Nguyen, D. Braig, A. Scholtissek, D. Ning, T. Li, A. Dreizler, C. Hasse, Ignition and kinetic-limited oxidation analysis of single iron microparticles in hot laminar flows, Fuel 371 (2024) 131866.
[18] W.E. Ranz, Evaporation from drops, Chem. Eng. Prog. 48 (1952) 142–180.
[19] J. O'Brien, J. Urzay, M. Ihme, P. Moin, A. Saghafian, Subgrid-scale backscatter in reacting and inert supersonic hydrogen–air turbulent mixing layers, J. Fluid Mech. 743 (2014) 554–584.
[20] M. Klein, A. Sadiki, J. Janicka, A digital filter based generation of inflow data for spatially developing direct numerical or large eddy simulations, J. Comput. Phys. 186 (2003) 652–665.
[21] A. Kempf, M. Klein, J. Janicka, Efficient generation of initial- and inflow-conditions for transient turbulent flows in arbitrary geometries, Flow Turbul. Combust. 74 (2005) 67–84.
[22] L. Engelmann, J. Hasslberger, S.J. Baik, M. Klein, A. Kempf, Direct numerical simulation of an unsteady wall-bounded turbulent flow configuration for the assessment of large-eddy simulation models, Sci. Rep. 13 (2023).
[23] L.C. Thijs, D. Ning, Y.S. Shoshin, T. Hazenberg, X. Mi, J.A. van Oijen, P. de Goey, Temperature evolution of laser-ignited micrometric iron particles: A comprehensive experimental data set and numerical assessment of laser heating impact, Appl. Energy Combust. Sci. 19 (2024) 100284.
[24] D. Ning, Y. Shoshin, J. van Oijen, G. Finotello, L. de Goey, Burn time and combustion regime of laser-ignited single iron particle, Combust. Flame 230 (2021) 111424.